Supporting Information

Mesoscale Polymer Regulation for Fast-charging Solid-State Lithium Metal Batteries

Yuetao Ma[a], Likun Chen[a], Yuhang Li[a], Boyu Li[a], Xufei An[a], Xing Cheng[a], Hai Su[a], Ke Yang[a], Guanyou Xiao[a], Yang Zhao[a], Zhuo Han[a], Shaoke Guo[a], Jinshuo Mi[a], Peiran Shi[a*], Ming Liu[a], Yan-Bing He[a*] and Feiyu Kang[a,b*]

a. Shenzhen All-Solid-State Lithium Battery Electrolyte Engineering Research Center, Institute of Materials Research (IMR), Tsinghua Shenzhen International Graduate School, Shenzhen 518055, China.

b. Laboratory of Advanced Materials, School of Materials Science and Engineering, Tsinghua University, Beijing, 100084, P. R. China.

Correspondence and requests for materials should be addressed to P.S. (shipeiran@sz.tsinghua.edu.cn) or Y.-B.H. (he.yanbing@sz.tsinghua.edu.cn) or F.K. (fykang@sz.tsinghua.edu.cn).

Experimental

2.1. Materials

PVDF (kynar 761, Mw=300,000) was bought from Arkema. PVA-203, KH550, DMF and STO nano-particles were provided from Aladdin. LiFSI came from Tinci Materials Technology Co., Ltd.

2.1. Preparation of PVA@STO

Typically, 1 g STO nano-particles, 6g PVA-203 and 2.5 g KH550 were dissolved in 45 mL H_2O and stirred at 85 °C for 24 h. The resulting suspension product was then centrifuged and washed with ethanol. The above steps were repeated three times to completely remove any residual PVA and KH550. After drying, PVA@STO was obtained.

2.2. Preparation of solid-state electrolytes

The PVDF, PS and PPS electroletes were prepared by a solution casting method. Typically, 400 mg PVDF, 267 mg LiFSI were dissolved in 10 mL DMF solvent and stirred at 25 °C for 6 h to obtain a homogeneous solution, then the PVA@STO nano-particles were added into the solution. The weight percentage of PVA@STO nano-particles in the total mass of PVA@STO nano-particles and PVDF was 10%. After that, the homogeneous mixture was poured into glass culture dish mold, drying for 14.5 h at 55 °C under an oven and stored in a glovebox for 24 h. The PVDF electroletes were prepared by a similar method without the PVA@STO nano-particles. The PS electroletes were prepared by a similar method, replacing PVA@STO with STO. The

thin PPS electrolytes were prepared similarly, with PVDF and LiFSI adjusted to 100 mg and 67 mg, respectively.

2.3. Fabrication of cell

Typically, 800 mg NCM811, 100 mg PVDF binder and 100 mg Super P were magnetically stirred in NMP solvent for 6 h at 25 °C. The resulting mixture was then cast onto aluminum foil. After drying at 80 °C, the mass loading of the cathode was approximately 1 mg cm^{-2}. All CR2032 batteries were assembled in an argon-filled glove box, using lithium metal as the anode and NCM811 as the cathode.

2.4. Materials characterizations

The scanning electron microscope (SEM) images of SSEs were obtained using a HITACHI S4800, equipped with energy dispersive spectroscopy (EDS) for elemental analysis. The atomic force microscopy-nano infrared (AFM-nano-IR) analysis was undertaken on a Bruker Anasys nanoIR2-fs instrument. The crystal structure of solid-state electrolytes (SSEs) was analyzed using X-ray diffraction (XRD) with Cu-Kα radiation on a Rigaku Smartlab. Fourier transform infrared (FTIR) spectra were collected in attenuated total reflection (ATR) mode using a VERTEX 70 spectrometer. A Bruker 400 MHz AVANCE NEO spectrometer was used for the solid-state ^{7}Li nuclear magnetic resonance (NMR) experiments. The stress-strain relationship of the electrolytes was characterized by the tensile strength taken from the maximum stress value of the stress-strain curve. Raman spectroscopy was conducted at room temperature using a Horiba LabRAM HR800 Micro-laser confocal Raman spectrometer (532 nm laser). Cross-sectional morphologies of cathodes and electrolytes

were observed using a focused ion beam-scanning electron microscope (FIB-SEM, FEI Helios G4 UC). The electron energy loss spectroscopy (EELS) mapping was carried out using a Thermo Fisher Scientific Spectra 300 cold-field-emission spherical aberration corrected transmission electron microscope, operated at 80 kV. The 3D distribution of the solid electrolyte interphase (SEI) was obtained using time-of-flight secondary ion mass spectrometry (TOF-SIMS, PHI nanoTOF II, 30 keV, 2 nA) in a 200 μm×200 μm×40 nm region after cycling Li||NCM811 batteries 50 times at 1C. Atomic force microscopy (AFM) was utilized to examine the surface morphology of the Li anode (MDTC-EQ-M16-03 Bruker Dimensionicon, Germany), along with X-ray photoelectron spectroscopy (XPS) performed using a PHI 5000 VersaProbe II instrument. Field emission transmission electron microscopy (FE-TEM) images of the CEI on the cycled NCM811 were obtained using a FEI Tecnai F30 instrument.

2.5. Electrochemical measurements

Under identical conditions, the electrochemical impedance of PVDF, PS, and PPS was evaluated using a VMP3 multichannel electrochemical station (Bio Logic Science Instruments, France). For the impedance measurements, small samples of PVDF, PS, and PPS were sandwiched between two stainless-steel blocking electrodes (SS-SS) in a coin cell, and the frequency was swept from 7 MHz to 0.1 Hz with a 10 mV AC oscillation. The ionic conductivities (σ) were calculated following Eq. (1).

$$\sigma = \frac{L}{RS} \tag{1}$$

Where L represents the thickness of different SSEs, R denotes the impedance of the SS/SSEs/SS cells at varying temperatures (from 25 to 95 °C), and S indicates the area of the SS blocking electrode. The activation energy was calculated following Eq. (2).

$$\sigma = \sigma_0 exp(-\frac{E_a}{RT}) \quad (2)$$

Where E_a represents the activation energy for ion transport, while σ_0 is the pre-exponential factor. Linear sweep voltammetry (LSV) was conducted from 0 to 7 V with a scanning rate of 0.1 mV s^{-1}. The galvanostatic charge and discharge tests were performed using Neware and LAND CT2001A systems, with a voltage range from 2.8 to 4.3 V at various rates (1 C = 180 mAh g^{-1}). In the 10 C test, the Li||NCM811 battery was first cycled for 3 cycles at each rate (0.2 C, 0.5 C, 1 C, 2 C, and 5 C), and then cycled at 10 C to achieve the 10 C test.

Finite element method

In this paper, we simulated the concentration profiles and overpotential distributions of the samples using the lithium-ion battery physics module in COMSOL Multiphysics software. The model was created based on the Electroneutrality Nernst-Planck equations as shown in equation S1-S5. c_i, J_i, D_i and z_i are the concentration of ion, ion flux, diffusion coefficient, charge number. u_i, F, ϕ and i_l represent electric mobility, Faraday constant, electrolyte potential and the electrolyte current density.

$$\nabla \cdot J_i = 0 \quad \text{S1}$$

$$\nabla \cdot i_l = 0 \quad \text{S2}$$

$$J_i = -D_i \nabla c_i - z_i u_i F c_i \nabla \phi \quad \text{S3}$$

$$\Sigma_i z_i c_i = 0 \quad \text{S4}$$

$$i_l = F\Sigma_i z_i J_i \quad \text{S5}$$

The electrode surface solved by The Butler-Volmer kinetic equation, as shown in equation S6. η, R, T, i_0, α_a and α_c are overpotential, the ideal gas constant, temperature, exchange current density, anodic transfer coefficient and cathodic transfer coefficient, respectively. Nernst-Einstein relation was used to defines the relation between D_i and u_i, which can be expressed as equation S7. In addition, we used equation S8 to define the electrolyte conductivity. Importantly, the normal deformation velocity of the electrolyte surface is defined by equation S9. V_n, i, M_i and ρ represent the normal deformation velocity surface current density, molar mass of the ion, and the density of the deposition material.

$$i = i_0\left(\frac{(\alpha_a + \alpha_c)F}{RT}\right)\eta \quad \text{S6}$$

$$u_i = \frac{D_i}{RT} \quad \text{S7}$$

$$S = \Sigma_i z_i^2 F^2 c_i u_i \quad \text{S8}$$

$$V_n = iM_i/\rho F \quad \text{S9}$$

Monte Carlo simulations

All MC simulations were performed with the LAMMPS[1] to investigate the crystallization behaviors of polymer systems grafted on $SrTiO_3$. VMD software was applied for trajectory visualization and analysis. The two systems respectively represent the interfacial growth system and the particle dispersion growth system. The first system comprises $SrTiO_3$, PVDF, and PVA. The second system comprises $SrTiO_3$ and PVA. The vacancy sites are regarded as solvent molecules, and then the simulation

systems can be treated as polymer solutions. The OPLS-AA force field was used for PVDF and PVA.[2] The force field parameters for $SrTiO_3$ were derived from simulation studies.[3] The non-bonded van der Waals interactions were molded using the 12-6 Lennard-Jones potential, while the electrostatic interactions, such as long-range Coulomb interactions, were addressed by the particle-particle-particle mesh technique.

The two system simulation boxes have a size of 6.37 nm × 5.07 nm × 6.37 nm and 12.0 nm × 12.0 nm × 12.0 nm, respectively, which contained 12 PVA and 34 PVA, respectively. In the production run, a time step of 0. 1 fs was used, and the data were collected every 1 ps. The system was minimized (atomic positions and cell sizes), keeping the box length isotropic. For each system, four independent trajectories of 1000 ps were generated. All production runs were employed the conventional metropolis sampling algorithm in each step of micro-relaxation with the potential energy penalty. Then an microcanonical ensemble at 298 K was performed to obtain the parametric of the system for 1000 ps. Periodic boundary conditions were applied in all directions.

Density functional theory (DFT) calculations

Density functional theory (DFT) calculations were performed with the generalized gradient approximation Perdew-Burke-Ernzerhof (GGA-PBE) functional. Projected augmented wave (PAW) potentials were chosen to describe the ionic cores, and valence electrons were considered using the plane wave basis set with a kinetic energy cutoff of 520 eV.[4-7] The electronic energy was considered self-consistent when the energy change was smaller than 10^{-4} eV per supercell. The geometry optimization was considered convergent when the residual forces were less than 10^{-2} eV $Å^{-1}$. For the

modeling description, the surface was simulated using the symmetric periodic slab model with consecutive slabs separated by a 15 Å vacuum layer.

Supplementary Figures

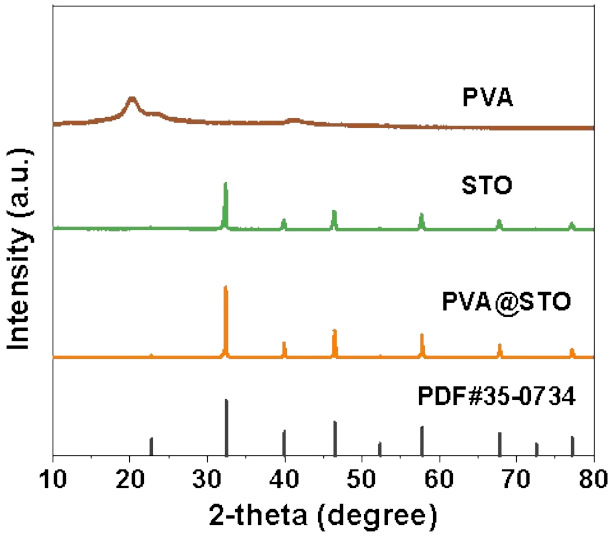

Fig. S1 XRD patterns of PVA, STO and PVA@STO.

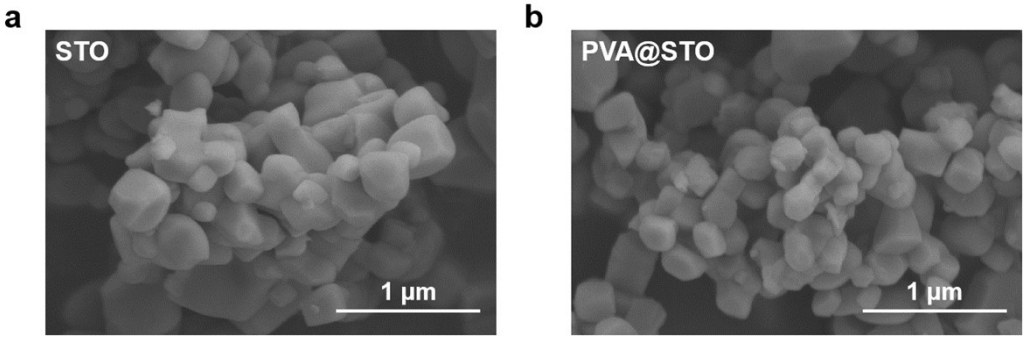

Fig. S2 SEM images of (a) STO and (b) PVA@STO.

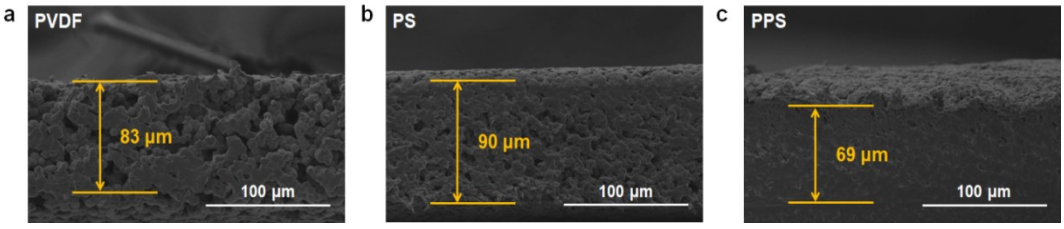

Fig. S3 Cross-section SEM images of the (a) PVDF, (b) PS and (c) PPS electrolytes.

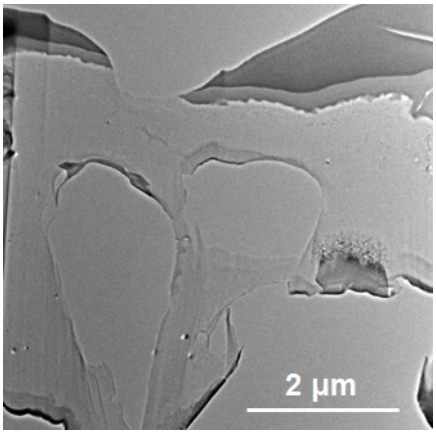

Fig. S4 TEM image of the PS electrolyte section.

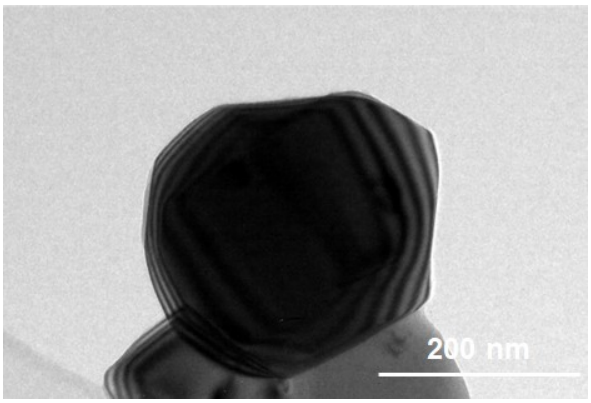

Fig. S5 TEM image of STO nano-particles.

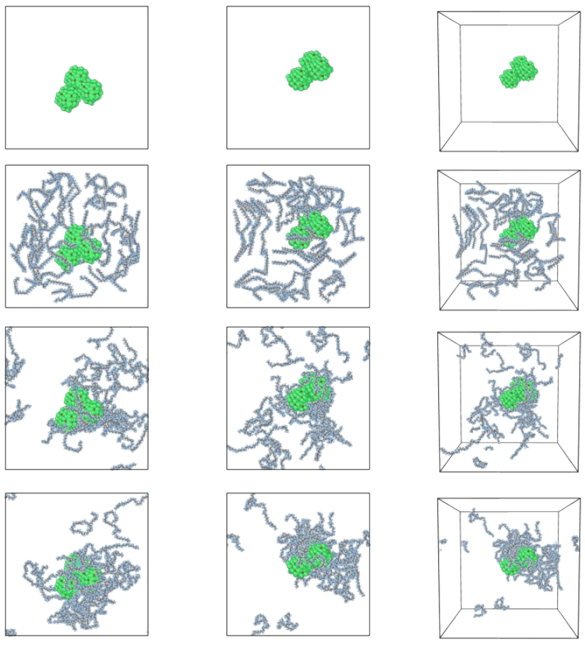

Fig. S6 Monte Carlo simulation of PVDF nucleation with agglomerate fillers.

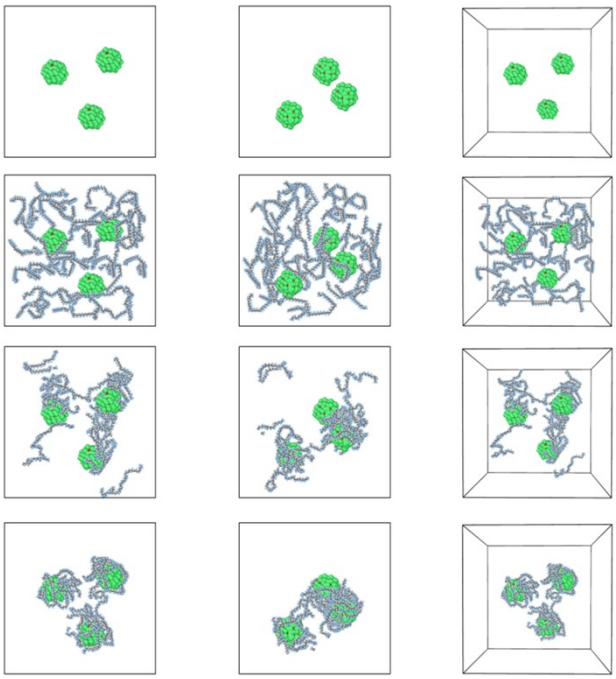

Fig. S7 Monte Carlo simulation of PVDF nucleation with dispersed fillers.

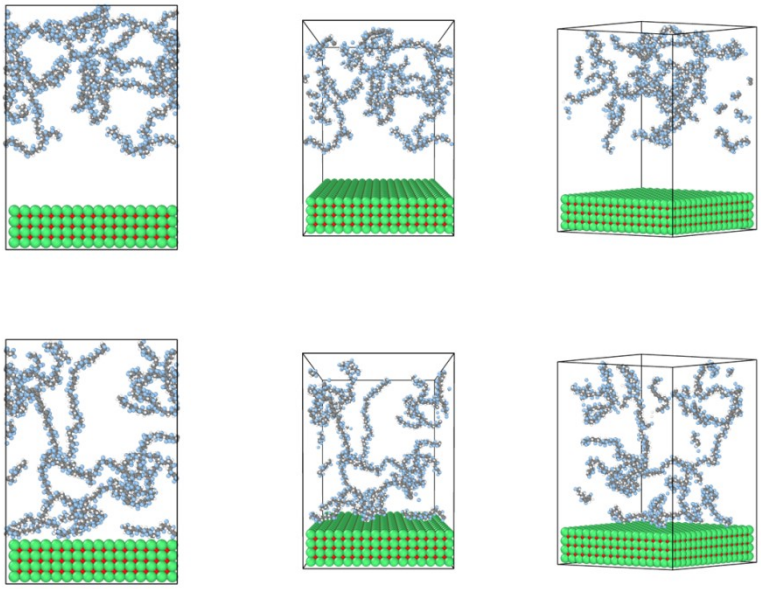

Fig. S8 Monte Carlo simulation of PVDF nucleation on STO surface.

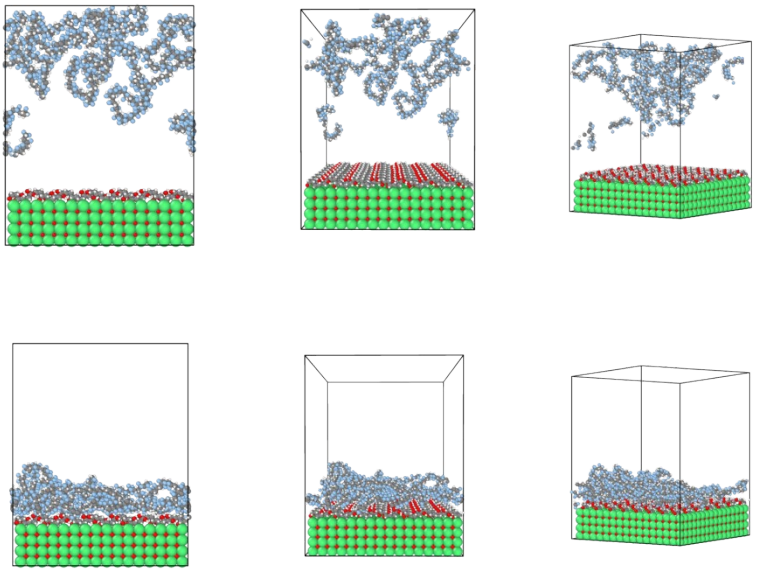

Fig. S9 Monte Carlo simulation of PVDF nucleation on PVA@STO surface.

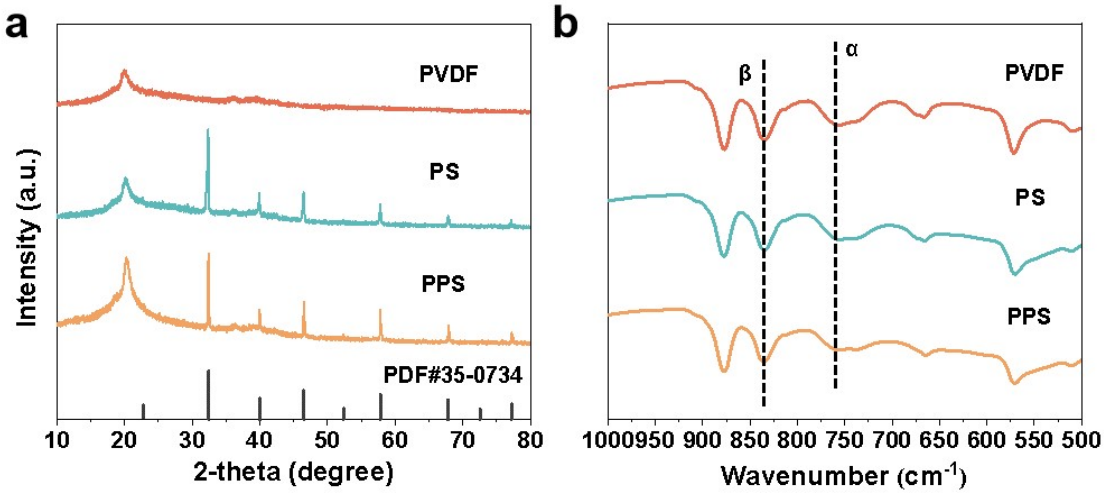

Fig. S10 (a) XRD patterns and (b) FTIR spectra of PVDF, PS and PPS electrolytes.

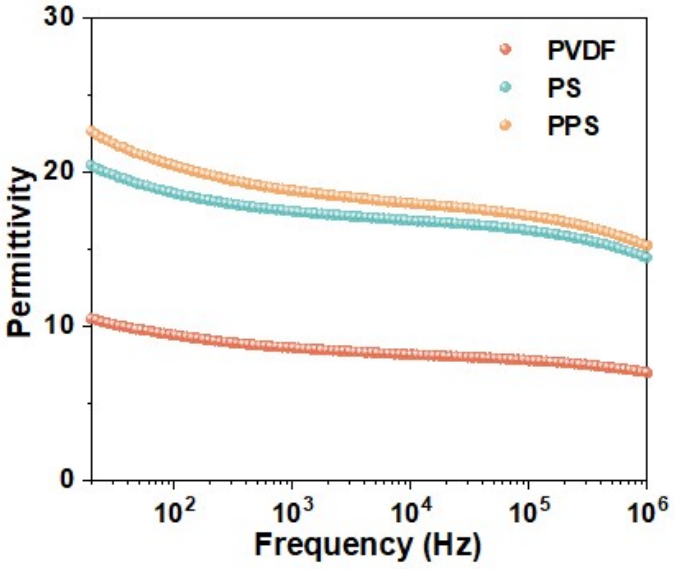

Fig. S11 Dielectric constants of PVDF, PS and PPS electrolytes.

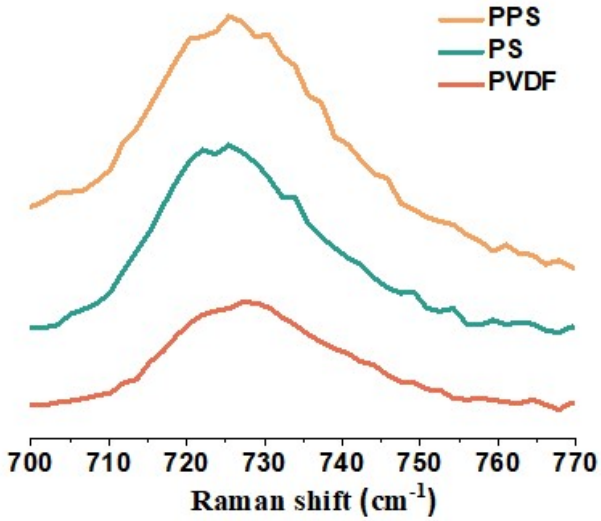

Fig. S12 Raman spectra of PVDF, PS and PPS electrolytes.

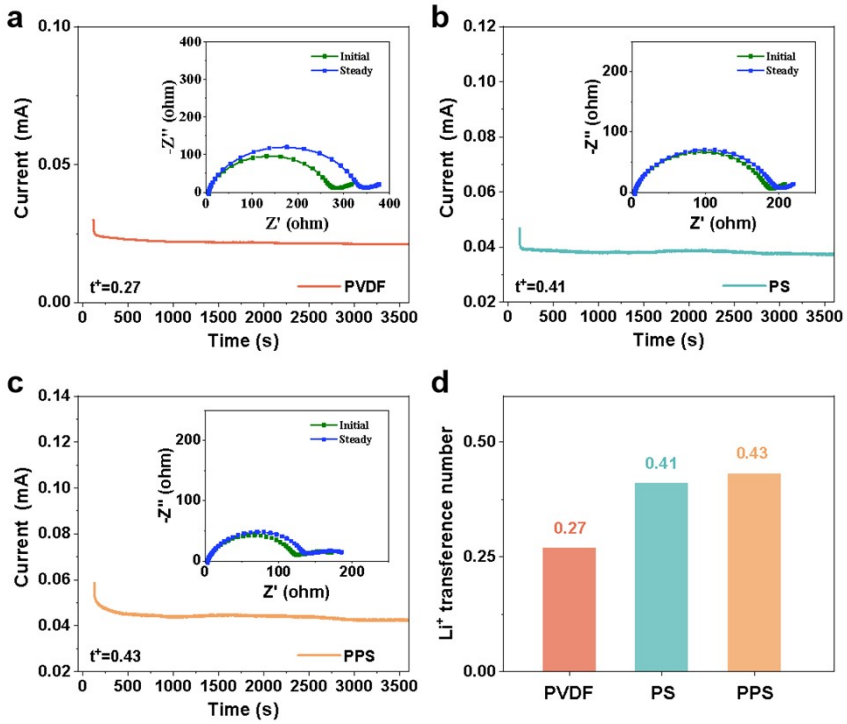

Fig. S13 Li^+ transference number of PVDF, PS and PPS electrolytes.

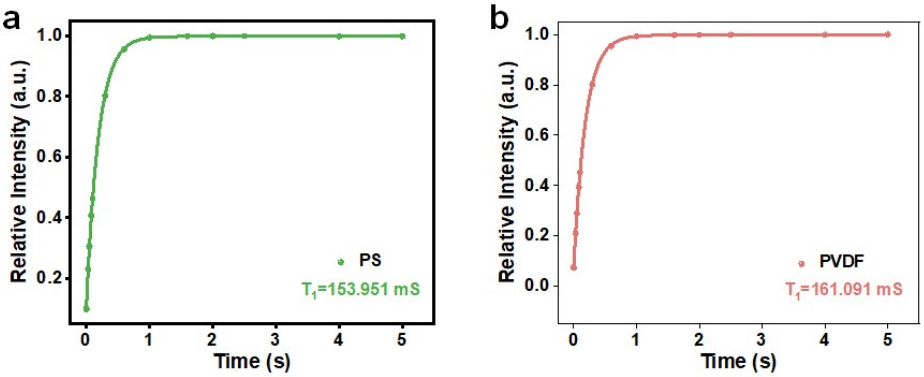

Fig. S14 T_1 of (a) PS and (b) PVDF electrolytes.

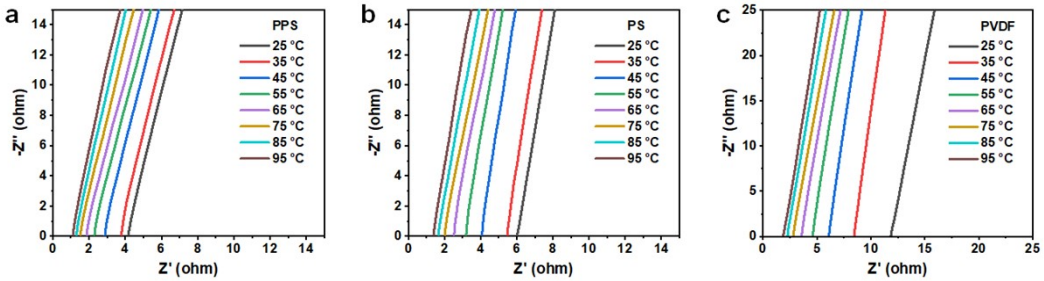

Fig. S15 Nyquist impedance spectra of stainless steel (SS)||SS batteries with (a) PPS, (b) PS and (c) PVDF electroletes.

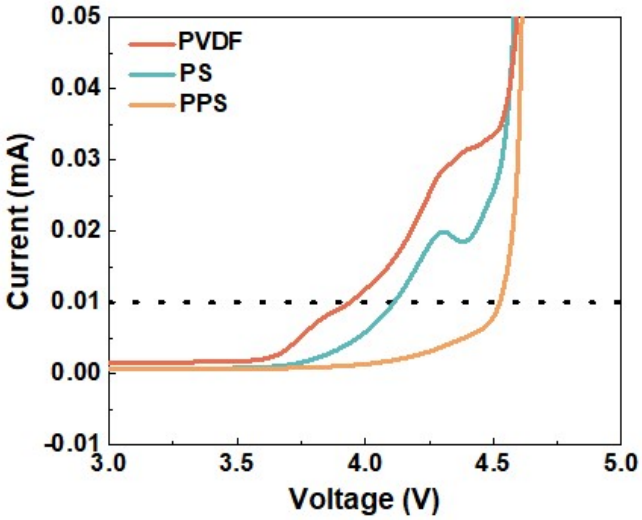

Fig. S16 LSV curves of the PVDF, PS and PPS electrolytes.

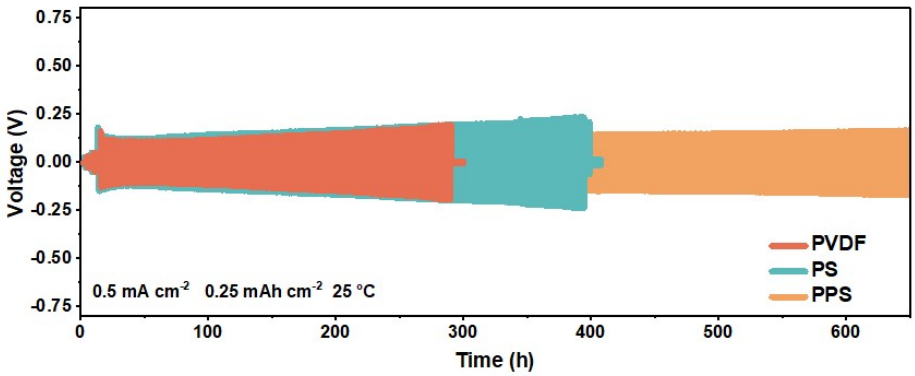

Fig. S17 Galvanostatic voltage profiles of the Li||Li symmetric batteries with PVDF, PS and PPS electroletes at 0.5 mA cm^{-2} and 0.25 mAh cm^{-2}.

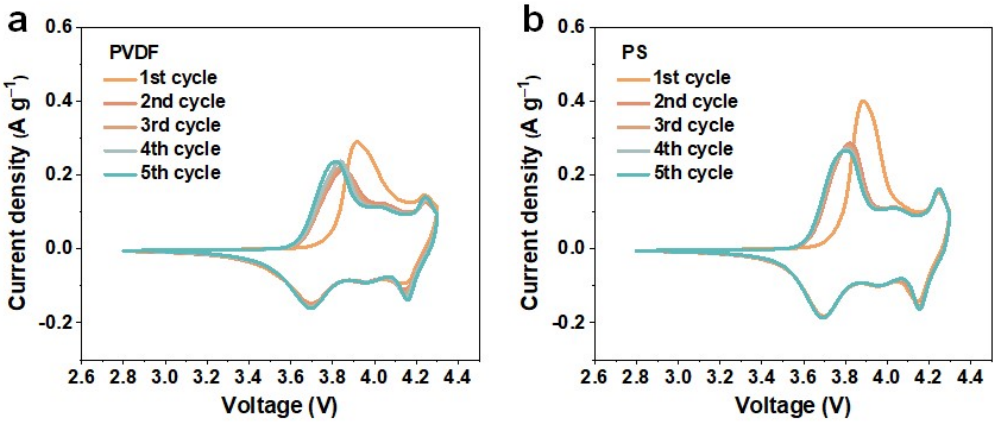

Fig. S18 CV measurements of the (a) Li|PVDF|NCM811 and (b) Li|PS|NCM811 batteries.

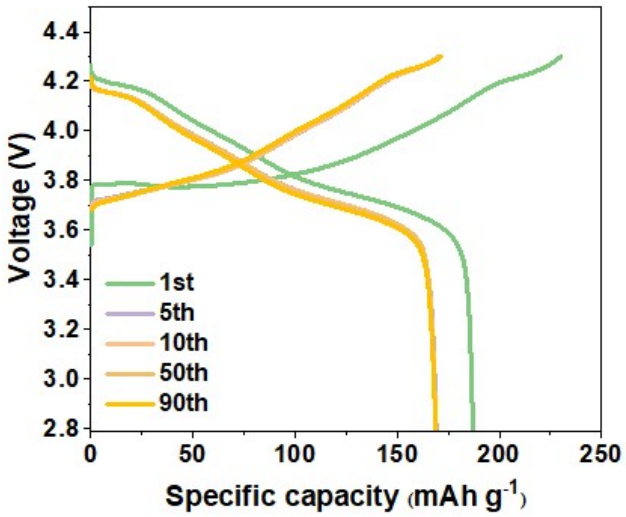

Fig. S19 Charge/discharge curves of Li||NCM811 battery with thin PPS electrolete.

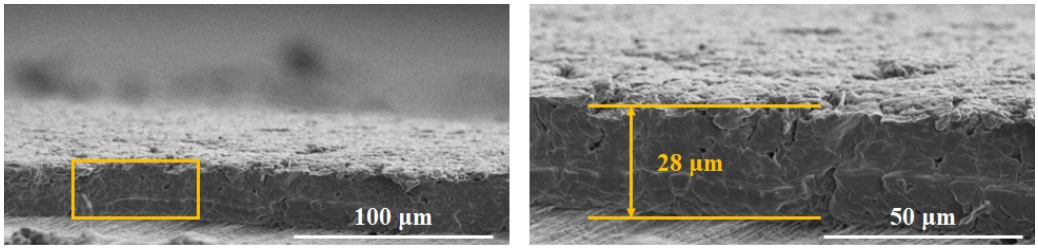

Fig. S20 Cross-section SEM images of the thin PPS electrolete.

Fig. S21 The thickness of the thin PPS electrolyte.

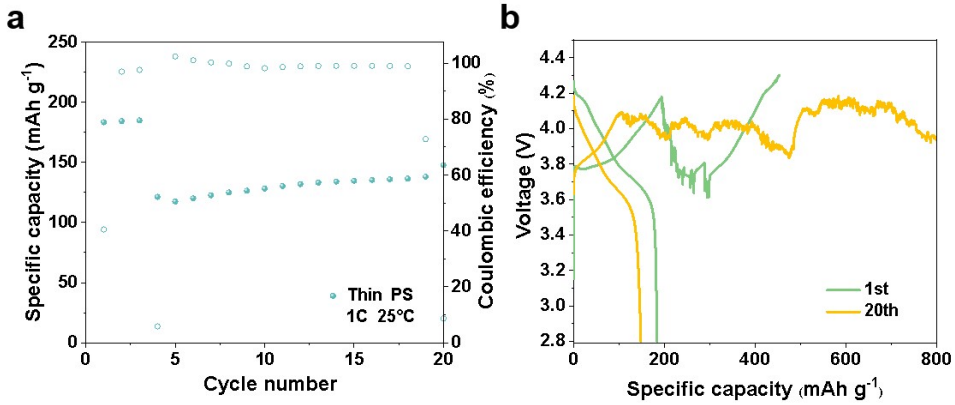

Fig. S22 (a) Cycling stability and (b) charge/discharge curves of Li||NCM811 battery with 28 μm PS electrolyte at 1 C.

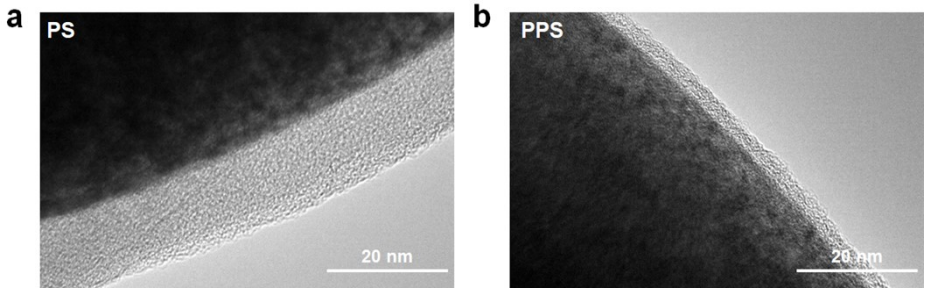

Fig. S23 TEM images of the CEI on cycled NCM811 with (a) PS and (b) PPS electrolytes.

Table S1. Comparison of solid-state Li||NCM811 batteries performance.

Electrolytes	Rate (C)	Cycle number	References
P(VDF-TrFE-CTFE)	0.5	150	*Energy Environ. Sci.* 2021, 14, 6021-6029
PVDF-$BaTiO_3$	0.5	250	*Energy Environ. Sci.,* 2024, 17, 3797-3806
PVDF-HFP-MOF	1	300	*Adv. Mater.* 2023, 35, 2310147
PVDF-LATP	1	500	*Angew. Chem. Int. Ed.* 2021, 60, 24668-24675
PVDF-zeolite	1	1130	*Angew. Chem. Int. Ed.* 2024, 63, e202401428
PVDF-$NaNbO_3$	1	1500	*Adv. Mater.* 2024, 36, 2311195
PVDF-LPPO	1	1550	*Energy Storage Mater.* 2022, 48, 375-383
P(VDF-TrFE-CTFE)-ILs	1	1600	*Angew. Chem. Int. Ed.* 2023, 62, e202300243
PVDF-C_3N_4	1	1700	*Nano Energy* 2022, 100, 107470
PVDF-C_3N_4	2	1500	*Nano Energy* 2022, 100, 107470
PVDF-LATP	2	1500	*Angew. Chem. Int. Ed.* 2021, 60, 24668-24675
PVDF-$MoSe_2$	2	2000	*Nat. Commun.* 2023, 14, 6296
PVDF-$MoSe_2$	3	2000	*Nat. Commun.* 2023, 14, 6296
PPS	5	2000	This work
PPS	10	2300	This work

Supplementary References

1. S. Plimpton, *J. Comput. Phys.*, 1995, **117**, 1-19.
2. H. Sun, *Macromolecules*, 1995, **28**, 701-712.
3. J. Crawford and P. Jacobs, *J. Solid State Chem.*, 1999, **144**, 423-429.
4. G. Kresse and J. Furthmüller, *Comput. Mater. Sci.*, 1996, **6**, 15-50.
5. G. Kresse and J. Furthmüller, *Phys. Rev. B*, 1996, **54**, 11169-11186.
6. J. P. Perdew, K. Burke and M. Ernzerhof, *Phys. Rev. Lett.*, 1996, **77**, 3865-3868.
7. P. E. Blöchl, *Phys. Rev. B*, 1994, **50**, 17953-17979.